Surface-roughened light-emitting diodes: an accurate model

Aurelien David

***Abstract*—Surface roughening is frequently employed to increase light extraction from light-emitting diodes (LEDs), especially in the important case of III-Nitride LEDs. We explore the physics governing this scheme. We introduce a numerical model, based on solving Maxwell's equations, to accurately describe scattering by a roughened semiconductor interface. This model reveals the complex angular dependence of the scattering properties. We then couple this approach to an LED light extraction model and predict how surface roughness impacts light extraction. We focus on two important cases, thin-film LEDs and volumetric LEDs. We show that optical losses in the LED dictate light extraction, and that volumetric LEDs offer an opportunity for ultimate efficiency.**

***Index Terms*—Light-emitting diodes, light extraction, scattering.**

CONTENTS

Aurelien David is with Soraa, Inc. Email: adavid@soraa.com

I. INTRODUCTION

As solid-state lighting emerges as a key technology for efficient lighting and energy conservation, [1] progress towards ultimate efficiency light-emitting diodes (LEDs) has become crucial. Light extraction efficiency is one of the main factors governing the external quantum efficiency of an LED. Generated light is naturally trapped by total internal refraction inside the high-index semiconductor of the LED. In order to enhance light extraction, the geometry of the LED has to be modified to break guided light trajectories and improve outcoupling.

Today, a few light-extraction schemes, shown on Fig. 1, dominate practical implementations:

• use of a patterned growth substrate (such as sapphire) which is kept in the final device, the patterned interface serving as a light scatterer.

• use of shaped chips for geometric randomization of light trajectories.

• use of surface roughness, most commonly in a thin-film geometry.

The first two approaches usually rely on large-scale features, and can safely be described by geometric optics. Surface roughness, on the other hand, frequently results in feature sizes of $100nm - 2\mu m$, and it is not clear that a geometric approach provides a proper description of the scattering behavior. Interestingly, although the surface-roughening approach is prevalent in high-power LEDs, little academic effort has been dedicated to describing it. Most of the available discussions of surface-roughened LEDs are experimental, and some present estimates for light extraction in real-world devices. The first implementations date back to GaAs LEDs [2] but renewed interest came with the need for high-efficiency III-Nitride LEDs [1], [3], [4].

From the theoretical side, academic work is scarcer. Apart from the use of geometric optics [5], trends on the use of surface roughness in optoelectronic devices have often been discussed in the framework of the 'photon gas model' based on Yablonovitch's seminal paper [6] whose key hypothesis is ergodicity – *i.e.* the assumption that after a few bounces light is randomized in the high-index medium and isotropically

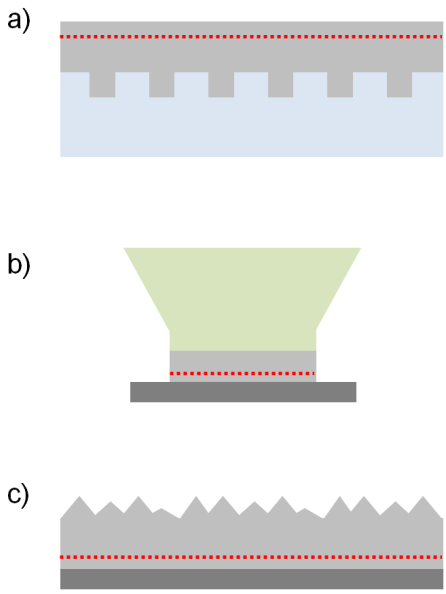

Fig. 1. Common light extraction schemes. a) Patterned sapphire substrate. b) Geometric approach (truncated inverted pyramid). c) Surface-roughened thin-film.

spans all propagation directions. This model has been successfully applied to the description of photovoltaic cells [7], [8]. Its application to LEDs, however, has been less frequent [2], [9]. We note that in Ref. [8], Yablonovitch *et al.* clearly state that the photon gas model is used for lack of a more accurate prediction of the angle-dependent properties of scattering.

A notable series of articles by Windisch and coworkers goes beyond the photon gas approach [10]–[12]. In these, the authors characterize experimentally the scattering properties of a textured GaAs interface by a variety of measurements, and inject the results in a light extraction model. The authors show that roughening an interface strongly modifies the angular dependence of one-bounce extraction and further randomizes light trajectories. As we will see, these conclusions are all in good agreement with ours. On the other hand, we note that the authors of this work were not able to measure the angle dependence of specular backscattering – which plays a critical role in our model.

In this article, we address quantitatively the issue of light extraction from surface-roughened LEDs with micron-size features. We first present a numerical optical model which accurately describes the scattering properties of a rough semiconductor interface. Based on this, we develop an accurate LED light extraction model and present selected predictions. As we will see, some of the results depart significantly from what could be derived in a photon gas model.

II. Light scattering by a rough surface

A. Approach

The statement of the scattering problem is summarized in Fig. 2. We consider a rough dielectric interface, which can be described by a few characteristic parameters, such as feature size, spacing and density. Given a plane wave with unit intensity, incident at polar angles θ and φ, we seek to

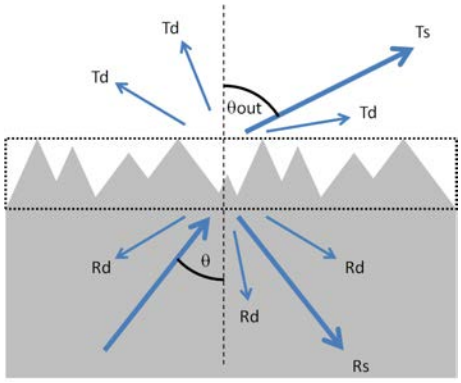

Fig. 2. Sketch of the scattering problem. The dotted box encompasses the scattering interface. The various scattering channels (specular and diffuse reflections and transmission) are shown. For simplicity, the sketch is restricted to a 2-dimensional geometry, but in practice azimuthal angles also intervene.

determine the following scattered intensities: R_s (specular reflection), R_d (diffuse reflection), T_s (specular transmission) and T_d (diffuse transmission). Energy conservation reads:

$$R_s + R_d + T_s + T_d = R + T = 1 \tag{1}$$

Here, R and T are the total (specular+diffuse) reflection and transmission intensities – in other words, T is the one-bounce extraction to the outside medium. R_d and T_d are the total diffuse intensities, obtained by integrating the angle-dependent diffuse intensities $R_d(\theta, \varphi, \theta', \varphi')$ and $T_d(\theta, \varphi, \theta', \varphi')$ over all outgoing solid angles $\Omega' \equiv (\theta', \varphi')$. We note that in literature, $R_d(\theta', \varphi')$ is sometimes called the Bi-directional Reflectance Distribution Function or BRDF [13].

All the quantities of Eq. 1 depend on θ and φ only. As we will show, the scattering properties are heavily dependent on θ but not on φ. Therefore, we will eventually describe all the above quantities as a function of θ only.

In principle, optical description of a random interface is difficult because one needs to consider a specific embodiment of the surface for numerical simulation. The question then arises whether the embodiment is representative of the random distribution, and whether the derived properties are relevant.

Our approach is as follows. We consider and model *periodic* corrugated interfaces whose characteristics (feature size, etc...) are similar to that of the random interface. By considering a number of configurations, we will see that some key scattering properties emerge which are common to all configurations and dominate the scattering behavior. Averaging over configurations will then provide us with an effective description of scattering by the random surface.

B. Scattering by a periodic corrugated interface

In practice, considering a periodic interface is advantageous because efficient numerical codes exist which can determine scattering properties exactly (modulo numerical truncation) by explicitly solving Maxwell's equations. In this article, we use the scattering-matrix (or S-matrix) approach, [14], [15] although other methods could be employed. We note that the periodic configurations we consider are also often called photonic crystals.

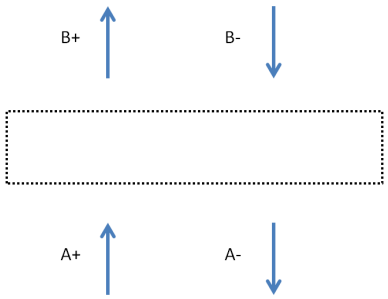

Fig. 3. S-matrix scheme. The dotted box represents the scattering interface. The incoming amplitudes are $A+$ and $B-$, and the outgoing amplitudes $B+$ and $A-$.

The problem of the the S-matrix scheme is described in Fig. 3. The amplitudes of the electric field are considered – each amplitude is a vector carrying field harmonics, indexed by their reciprocal lattice vector **G**. In principle the vectors are of infinite length, but they are truncated to a finite size for numerical implementation. The S-matrix relates the incident and outgoing field amplitudes at either side of the scattering object by:

$$\begin{bmatrix} B^+ \\ A^- \end{bmatrix} = S \cdot \begin{bmatrix} A^+ \\ B^- \end{bmatrix} \tag{2}$$

In our case $B^- = 0$ and A^+ is a plane wave (i.e. only the fundamental harmonic $\mathbf{G} = 0$ carries incoming power). Solving the problem straightforwardly yields the scattered amplitudes. The intensities are then obtained by squaring the amplitudes. The specular component of each intensity corresponds to the fundamental harmonic $\mathbf{G} = 0$, while the other harmonics constitute the diffuse component. Each of these harmonics corresponds to an outgoing solid angle $\Omega' \equiv (\theta', \varphi')$ and the total diffuse intensity is obtained by summing over the harmonics. For instance:

$$R_s = \left|A^-(\mathbf{G} = 0)\right|^2 \tag{3}$$

$$R_d = \int R_d(\theta', \varphi') d\Omega' = \sum_{\mathbf{G} \neq 0} \left|A^-(\mathbf{G})\right|^2 \tag{4}$$

We note that, because of the randomization by the rough surface, we will work with the field intensities rather than their amplitudes – i.e. we will make the reasonable hypothesis that phase is scrambled by the corrugation so that intensities of different scattering events can be summed in light extraction calculations.[1]

To illustrate our procedure, we first use a simple geometry. We consider a periodic corrugation in a GaN/air interface (Fig. 4). The corrugation is a triangular lattice of pitch a made of cylindrical rods of GaN (index $n = 2.4$) of height $h = 1$, and surface filling fraction $f = 0.3$, at an optical frequency $u = a/\lambda = 1$ (all distances are cast in units of a, as is customary in the field of diffractive optics). This configuration can be considered as moderate in terms of scattering efficiency. Here and in the remainder of Section II, we show results for TE polarization, although all the arguments apply equally to TM polarization.

[1]More precisely, we expect that while resonance effects may exist in the corrugated interface for a given round-trip of light, such effects will cancel out when averaged over multiple round-trips because light visits a slightly different configuration of the surface at each round-trip.

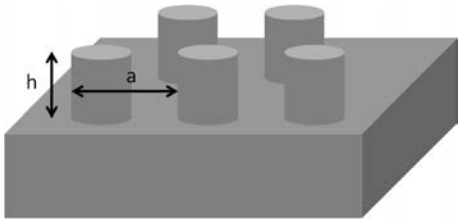

Fig. 4. Geometry of the periodic corrugated interface.

Fig. 5a displays the backscattered intensity $R = R_s + R_d$ versus the polar angle θ, for various azimuthal angles φ. Various values of φ yield different scatterings, because specific harmonics of the reciprocal lattice diffract at specific values of φ. However, the $\theta-$dependence of the scattered intensities is overall similar for all values of φ. Most notably, R converges to unity at glancing angles $\theta \sim \pi/2$.

C. Averaging over configurations

By averaging the scattered intensities over φ, we obtain the thick line shown on Fig. 5a. This represents the average optical response of the corrugation to light emitted at all azimuthal angles.

We now consider various values of u over the range $0.8 - 1.2$. Since Maxwell's equations are expressed as a function of the reduced wavelength $u = a/\lambda$, these variations can be considered as variations in the lattice period and/or in the wavelength of light. The scattered intensities (averaged over φ) are depicted on Fig. 5b. Again, variations occur for specific values of u but a dominant dependence on θ emerges, with R converging to unity at glancing angles for all configurations. The thick line in Fig. 5b shows the scattering intensities averaged over u.

Finally, we consider various rod heights h over the range $0.6 - 1.4$. Fig. 5c shows the scattered intensities (averaged over φ and h). Once more, we observe small variations in the details of R, which are due to vertical (Fabry-Pérot-like) resonances in the vertical direction of the rods. However all curves share a rather similar shape and are dominated by the $\theta-$dependence.

The averaged backscattered efficiency is plotted with a thick line in Fig. 5c. The resulting curve has been averaged over φ, u and h. Obviously the result depends on the ranges considered for averaging. However, as we have seen, variations are small and slow over a rather wide range of parameters. It can be checked that using other averaging ranges yields a similar final result, provided the magnitude of u and h does not vary wildly. Therefore, if we consider a random corrugation whose geometric parameters span a reasonably well-defined range, our averaging approach should result in a representative scattering behavior.

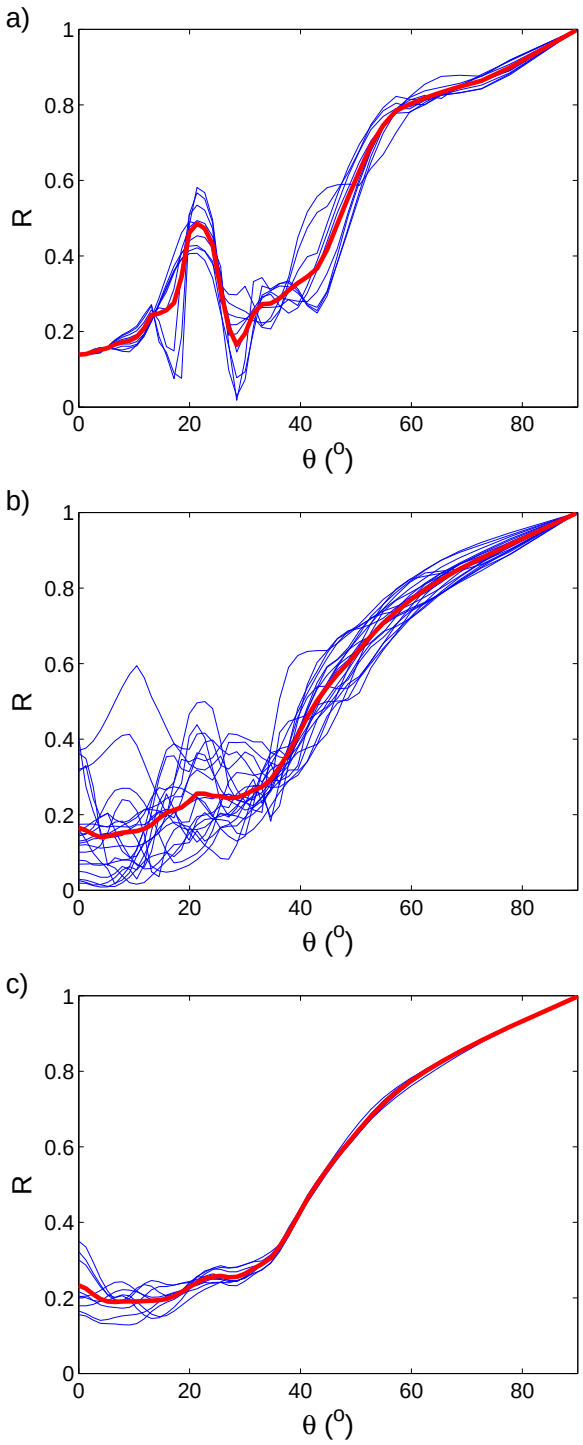

Fig. 5. Total backscattering R vs. θ for various configurations. In each case the thick line is the average over the thin lines, which represent different configurations. a) Varying azimuthal angles $\varphi = 0-2\pi$, for $u = 1$ and $h = 1$. b) Varying $u = 0.8 - 1.2$, after averaging over φ. c) Varying $h = 0.6 - 1.4$ after averaging over φ and u.

D. Scattering strength

So far we have kept the filling fraction f of the rods constant. Fig. 6 shows R and R_s (averaged over φ, u and h) for various values of f. Unlike other parameters, f significantly modifies the result. In the case $f = 0$ (where the interface is smooth) R and R_s coincide with the Fresnel reflection coefficient. For small values of f, R and R_s are still reminiscent of the Fresnel coefficient, but some extraction is allowed beyond the critical angle where R becomes smaller than 1. For larger values of f, R is significantly modified and strong scattering occurs. Because of this behavior, f can be used as a parameter to vary the extraction efficiency of a rough surface.

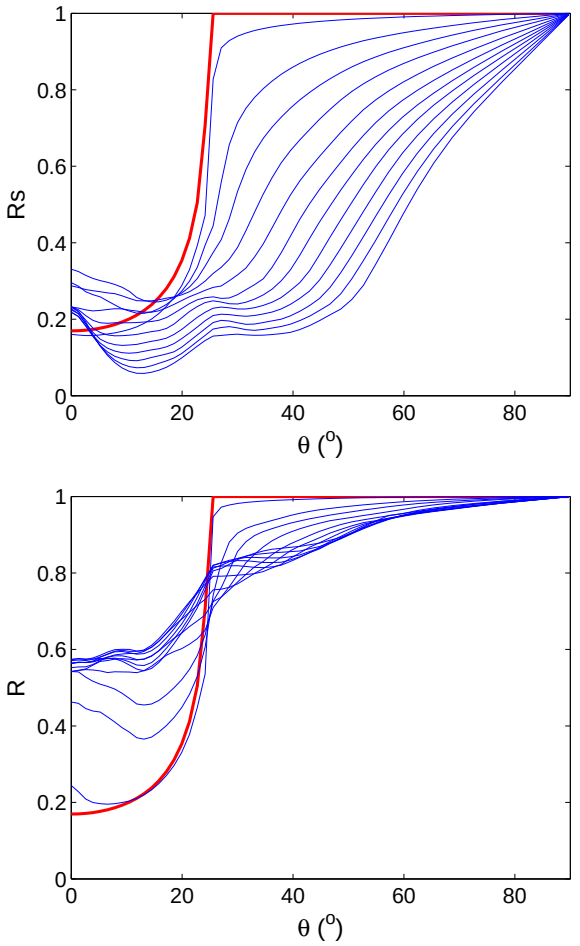

Fig. 6. Scattering vs. filling fraction f of the rough surface (varying from 0 to 0.6 in steps of 0.05). Top: specular reflection R_s. Bottom: total backscattering R. The thick line corresponds to $f = 0$ and coincides with the Fresnel reflection coefficient for a planar interface.

By integrating the transmission $T = 1-R$ over solid angles, we can also compute the one-bounce extraction efficiency of the textured surface. In the case of Fig. 6 we find that this value increases from 6.5% for a smooth surface, to 9.5% for a surface with large f. This is due to the increased extraction at large solid angles, which more than compensates the increased backscattering near normal incidence. This prediction is in line with the measurements of Ref. [12].

We also notice that our results depart from those one would obtain in a geometric optics approach. This will be discussed further in Appendix A.

Here, we note that our scattering model does not aim at prescribing what average over configurations properly describes a specific rough surface. Instead, our approach enables us to generate a family of *realistic* scattered intensities with vary-

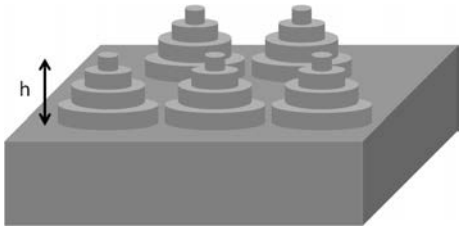

Fig. 7. Geometry of a roughened surface made of conical pyramids.

ing scattering strengths (implicitly controlled by f). Where quantitative agreement with experimental data is sought, one needs to calibrate the model by determining which scattering strength best describes the set of existing experimental data. This procedure has been used to model our experimental results, and has shown excellent accuracy.

E. Robustness of the averaging approach

As we will now check, these emergent scattering properties are actually robust and do not depend strongly on the details of the corrugation's geometry.

1) Cylinders vs. pyramids: As a first example, we compare the results obtained previously for cylindrical scatterers with pyramidal (conical) corrugations. Pyramidal features are of practical interest as they closely mimic the surface roughness typically obtained by chemical etching of a GaN surface. The pyramids are approximated by a set of 10 slices, as sketched on Fig. 7. We assume the same filling factor $f = 0.3$ for the cylindrical rods and the base of the pyramids. In both cases, we average over the azimuthal angle φ and frequency u. For the cylindrical rods we average over h. For the pyramids on the other hands, we maintain the pyramids' angle at 60^o (corresponding to the conical features observed in roughened GaN) so that h is fixed.

Fig. 8 compares the scattered efficiencies after averaging. As can be seen, the results are nearly identical. It can be checked that for other values of f, pyramids and rods still have a similar behavior. From this we conclude that the details of the corrugation's shape are not critical for the emergent dependence of scattering on θ.

2) Supercell: All the results shown so far pertain to periodic corrugations. We have argued that statistical averaging enabled us to describe the effect of randomness. However, one can wonder if the results we obtained are tied to using a simple periodic cell with one scatterer, and whether more short-scale disorder would break down these trends.

To address this question, we extend our calculations to a supercell approach. The problem is still periodic, but several scatterers of various shapes are now included in a unit cell so that order on the scale of a wavelength is lost. Specifically, the unit cell now comprises three types of pyramids of filling fractions $f = 0.4$, $f = 0.17$ and $f = 0.02$. The corresponding geometry is shown on Fig. 9: the pyramids of various sizes now cover the whole surface.

Fig. 10 shows the result of this calculation, compared to a simple periodic cell with one pyramid of filling fraction $f = 0.4$ ($i.e.$ retaining only the larges pyramids from the previous surface). As can be seen, both results are again quite similar, because the details of the corrugation do not strongly influence the scattering behavior.

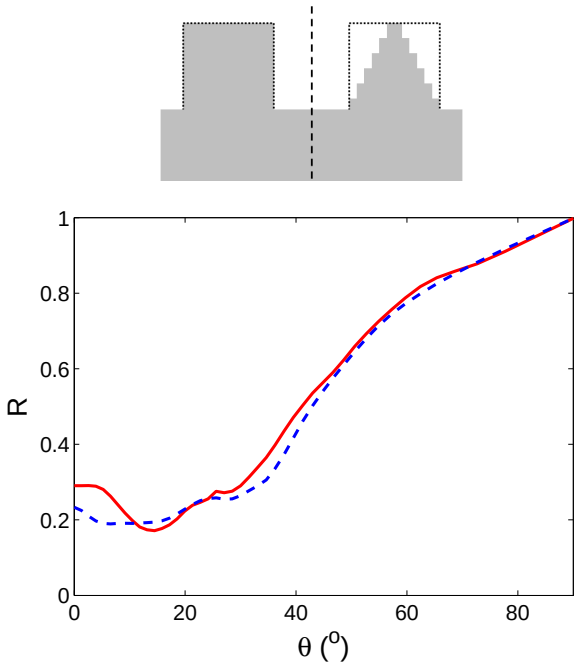

Fig. 8. Averaged backscattering for two geometries: rods and pyramids. Top: sketch of the respective geometries. The base filling factor of the pyramids is equal to the filling factor of the rods. Bottom: backscattering vs. θ. Full line: pyramids; dashed line: rods.

From this we conclude that the present results are not related to using a simple one-scatterer cell. Following this approach, we can increase the reduced frequency u to model unit cells of larger lateral extent. We have pushed our calculations to $u = 2$ and still observed similar trends in the scattering profiles. For this value of u, the largest pyramids in Fig. 9 have lateral dimensions $\sim 1\mu m$ and the modeled surface is representative of a typical roughened GaN surface.

In principle, one could keep extending the dimensions of the supercell (although in practice, computation time makes this impractical) to approximate a higher degree of disorder. The key trends of the scattering profile are still expected to hold because they do not rely on the details of the roughness, as we will justify in Section II-H.

F. General trends of scattering

Having established a method to derive representative scattering functions for a rough surface, we now look in more details at our results.

Fig. 11 plots the breakdown of the forward- and backscattering efficiencies, with the details of the specular and diffuse components. Here we consider a surface made of cones with base filling fraction $f = 0.3$, and averaged over $u = 1.5 - 2$. As already discussed, backscattering reaches unity at high angles. Near normal incidence backscattering is mostly diffuse, but this diffuse component vanishes at large angle where backscattering becomes mostly specular. It is also instructive to consider the equivalent forward-scattering quantities, which

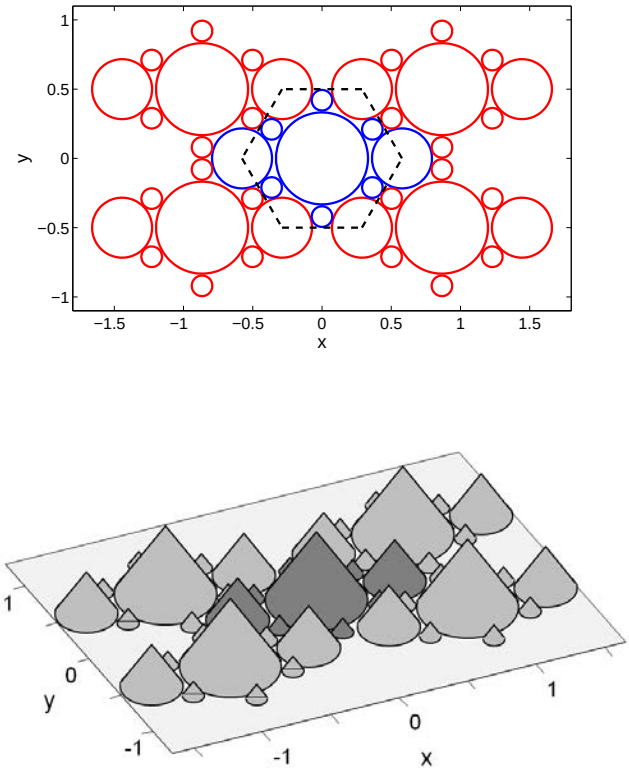

Fig. 9. Geometry of a roughened surface with a large unit cell (supercell). Top: top view of the supercell. The circles represent the base of each pyramid. The dashed lines mark the boundaries of the unit cell. Bottom: perspective sketch of the surface. The darker pyramids corresponds to the unit cell. All distances are in units of the lattice pitch a.

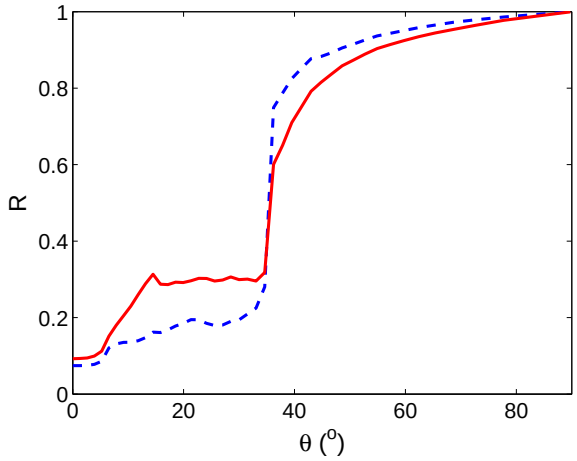

Fig. 10. Averaged backscattering R for two geometries: simple cell including only one pyramid with $f = 0.4$ (dashed line) and supercell including a variety of pyramids (full line). Despite small deviations, the trends are similar. Here the frequency is $u = 1$ and the outside medium is an encapsulant ($n = 1.4$).

correspond to one-bounce extraction from the rough surface. Transmission is mostly specular near vertical angle where light is in the extraction cone ($\theta < \theta_c$), and becomes only diffuse at large angle. From this, we get more insight in the existence

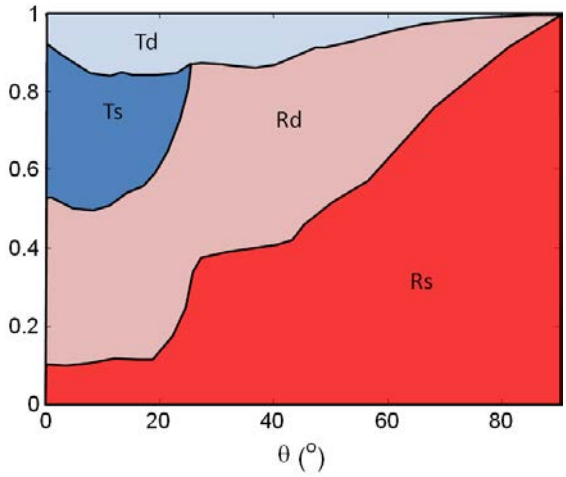

Fig. 11. Breakdown of scattering channels in a typical case. R_s and R_d are the specular and diffuse reflections, T_s and T_d are the specular and diffuse transmissions.

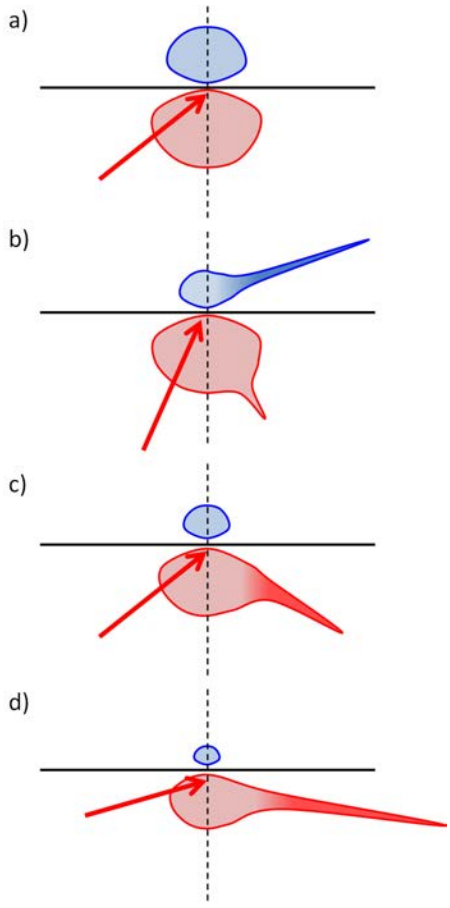

Fig. 12. Sketches of scattering profiles for various cases. The horizontal line represents the rough surface, and the clouds are the backward and forward-scattered intensities. a) Ideal diffuser, with no specular peaks in the scattering profiles; Lambertian diffusers fall under this category. b-d) Realistic scattering at various angles of incidence. b) near normal incidence T is mostly specular and R is mostly diffuse. c) At intermediate angles T is diffuse and the specular component of R increases. d) At glancing angle T vanishes, and R is mostly specular.

of kinks in scattering near the critical angle: for $\theta > \theta_c$

specular transmission (corresponding to the fundamental harmonic $\mathbf{G} = 0$) is not allowed and only diffuse transmission contributes to light extraction.

Fig. 12 summarizes these calculations with sketches of the scattering profiles for various angles of incidence.

We note that qualitatively similar diagrams can be found in scattering studies performed in the field of computer graphics theory, where accurate descriptions of scattering by diffuse surfaces are required for realistic computer rendering. In this field, it has long been known that large-angle scattering was composed of a diffuse and a specular (or quasi-specular) components [16]–[18]. However, to our knowledge, such effects have not been considered in optoelectronic devices – and more generally in a situation where light comes from a high-index medium and can be both transmitted and reflected.

G. Encapsulation

High-index encapsulation ($n \sim 1.4 - 1.5$) is often used to increase light extraction. The effect of encapsulation is obvious for a smooth LED: it enlarges the extraction cone by a factor $\sim n^2$ for each facet. However, the effect is more subtle for surface-roughened LEDs since scattering is heavily dependent on the optical indices of the inner and outer media. Qualitatively, encapsulation has two effects. First, it opens the extraction cone – in principle this concept only applies for a smooth interface; however it retains some relevance for roughened surfaces, as we have explained in Section II-F. Second, encapsulation reduces the index contrast Δn between the dielectric and the outside medium, therefore decreasing the scattering strength of the rough surface. This second effect can be significant: at least for small Δn, scattering efficiency scales with $\sim \Delta n^4$ [19]. The first effect favors light extraction, while the second decreases it. Photon gas models only take into account the first effect.

Fig. 13 shows how encapsulation into a medium of index $n = 1.4$ modifies the scattering properties. Here, the geometry is a set of pyramids, averaged over $u = 1.5 - 2$. We consider two scattering efficiencies $f = 0.1$ and $f = 0.3$, and show the total backscattering R.

For the weak scattering case $f = 0.1$, the result is reminiscent of the Fresnel reflection coefficient (which corresponds to $f = 0$). The effect of encapsulation is mainly to widen the extraction cone, as would happen with a smooth interface; both for extraction to air and to the encapsulant, there is only little single-pass outcoupling beyond the critical angle. It the strong scattering regime $f = 0.3$ on the other hand, encapsulation has a more complex and non-trivial effect: outcoupling is significantly enhanced at all angles.

Overall, it is apparent that encapsulation tends to increase the efficiency of scattering – this is because the additional channels for scattering in the high-index encapsulant overcome the decrease in index contrast. The net impact of encapsulation on light extraction will be discussed further in Section III-D3.

H. Physical origin of the $\theta-$dependence

The key result of our study is that the scattered efficiency is heavily dependent on the incoming angle θ: at glancing angles the reflection becomes mostly specular, while the diffuse components vanish. Here we discuss a possible way to physically interpret this result.

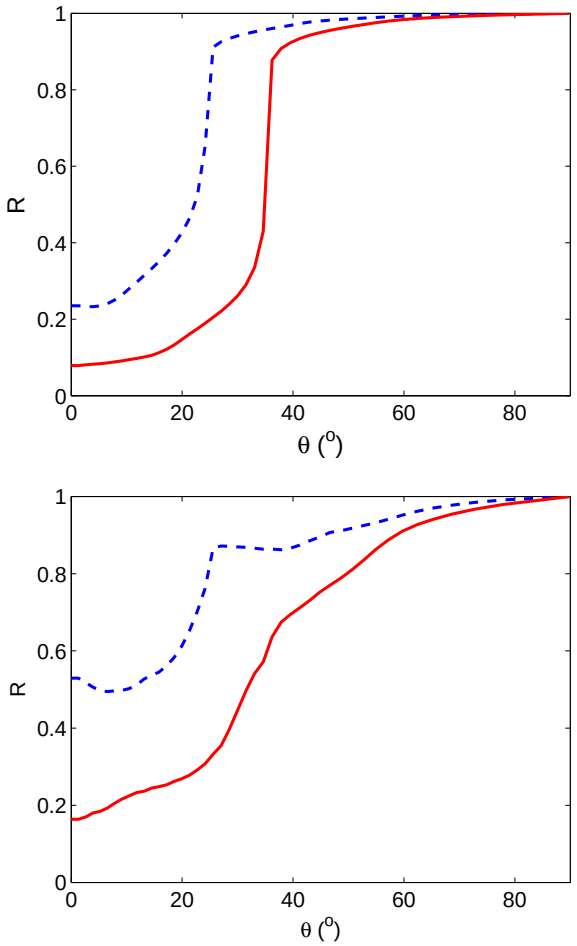

Fig. 13. Impact of encapsulation on backscattering R. Top: $f = 0.1$, bottom: $f = 0.3$. Full line: $n = 1$, dashed line: $n = 1.4$. Encapsulation can both widen the extraction cone and increases diffuse scattering beyond the extraction cone.

The incoming field is a plane wave, of in-plane wavevector $k_{//}$. Inside the texture layer, the field can be decomposed as a Fourier sum:

$$E(z) = \sum_G E_G(z, k_{//} + \mathbf{G}) \tag{5}$$

In the case of a periodic corrugation the sum is discrete (the **G**'s index the reciprocal lattice) while in a non-periodic corrugation it is continuous. However, in both cases the fundamental $E_0(z)$ tends to carry the majority of the power[2] and its vertical profile across the corrugation drives the scattering efficiency [19], [20].

In any Fourier decomposition of Maxwell's equation, the vertical propagation of this fundamental harmonic is governed by a Helmholz-like wave equation[3] in a medium described by

[2]Except under special excitation conditions such as excitation of a grating anomaly, but these correspond to narrow and specific angular ranges.

[3]With additional coupling terms to other harmonics, which are small.

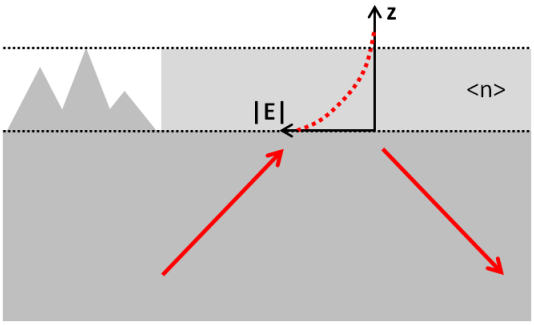

Fig. 14. Field penetration in a rough interface. The profile of the fundamental is shown inside the rough region, which to first order can be treated as an effective medium of index $\langle n \rangle$. For large incidence angles, the fundamental is evanescent which limits scattering efficiency.

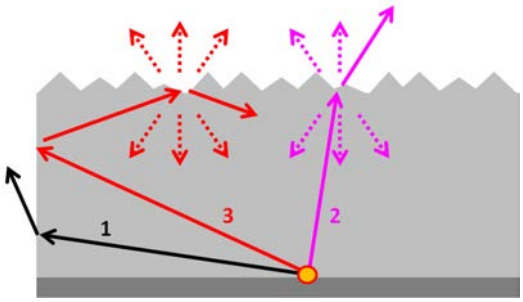

Fig. 15. Sketch of possible light trajectories in a surface-roughened LED. Ray 1 sees the flat sidewall of the LED near normal incidence and is extracted. Ray 2 sees the rough surface of the LED near normal incidence; it is largely extracted in a specular direction, and also diffusely scattered forward and backward. Ray 3 is at an intermediate angle; it is not extracted laterally and impinges on the rough surface at a large angle, so that it mostly undergoes specular reflection and little scattering.

an average optical index $\langle n \rangle$.[4] The exact value of $\langle n \rangle$ is not trivial, and should be derived from effective medium theories; however its order of magnitude is $\langle n \rangle^2 \sim f n_{in}^2 + (1-f) n_{out}^2$ where n_{in} and n_{out} are the indices of the core material and outer medium, and f the average filling fraction of the core material. The fundamental E_0 is characterized by an in-plane wavevector $k_{//}$, or equivalently by an effective index $n_{eff} = k_{//}/k_0 = n_{in} sin(\theta)$. For large values of θ, $n_{eff} > \langle n \rangle$ and E_0 is evanescent in the vertical direction. Larger values of θ correspond to faster exponential decays, *i.e.* a lesser penetration of E_0 in the corrugated region. Fig. 14 illustrates the profile of E_0 across the structure.

Since the overlap of E_0 with the corrugation drives scattering, large angles are weakly scattered by the rough surface. In the limit $\theta \to \pi/2$, the penetration of E_0 vanishes and so does scattering. This argument helps us understand why the results we obtained are so robust against the details of the roughness (feature size, shape...). Indeed the evanescent decay of E_0 only depends on the average index of the rough layer, which is not strongly dependent on its detailed configuration.

We note that this argument based on an average index approach is quite generic. For instance, it applies not only to random textures but also to periodic corrugations, $e.g.$ photonic crystals. This point is developed in Ref. [21], where we show that despite the apparent differences in optical behavior (discrete Bloch modes in photonic-crystal LEDs vs. diffuse angular distribution in random-textured LEDs) the same angle-dependent behavior applies to both cases, thus leading to similar extraction efficiencies (given a similar magnitude of optical loss). Notably, the well-known difficulty to extract low-order guided modes in photonic crystal LEDs (Refs. [19], [22], [23]) is equivalent to the poor extraction efficiency of large-angle light we have just described.

III. Modeling of LED light extraction efficiency

In this section, we employ the scattering properties we have derived to predict extraction efficiency trends for surface-roughened LEDs. We first consider an idealized LED of infinite extent to derive general extraction trends. We then study realistic thin-film chips. We conclude with roughened volumetric chips.

A. Qualitative discussion

We can expect that the dependence on θ will dominate the properties of light extraction by a rough surface. Fig. 15 shows a sketch of light trajectories at various angles θ in an LED. At small angles (near vertical), light is efficiently extracted after only one bounce. At large angles, light is efficiently extracted by the sidewalls provided it can reach them (which depends on the aspect ratio of the LED). For rays which impinge on the rough surface at intermediate and high angles on the other hand, light is poorly extracted *and mostly specularly reflected*, so that a large fraction of the power still propagates at large angles after several bounces. We can anticipate that extracting this light will be challenging. Obviously, this effect is not captured in a photon gas model where ergodicity is assumed. Rather, a proper description of surface scattering needs to integrate the $\theta-$dependence of scattering properties.

B. Ideal surface-roughened LED: ergodicity and number of bounces

To first illustrate our point, let us consider an idealized surface-roughened LED of infinite lateral extent emitting into air. The only source of loss is the $p-$mirror, of reflectivity $R_p = 95\%$ at all angles. In this geometry, the height of the LED is irrelevant.

Due to the infinite lateral extension of the system, the light propagation problem is one-dimensional and can be solved analytically. We call $I(\theta)$ the radiation diagram of the source, *i.e.* the amount of light emitted at an angle θ by the LED's active region (isotropic for our example). I is a column vector whose elements correspond to the angles of propagation. S is the single-bounce backscattering matrix of the rough interface obtained from our scattering model, such that $S \cdot I$ is the column vector of backscattered light if intensity I impinges on the rough surface.[5] We label by N the number of bounces

[4] In general $\langle n(z) \rangle$ varies with z but this does not affect our qualitative discussion.

[5] Formally, the scattering matrix used here is S_{21} e.g. the lower-left quadrant of the full $S-$matrix defined in Eq. 2.

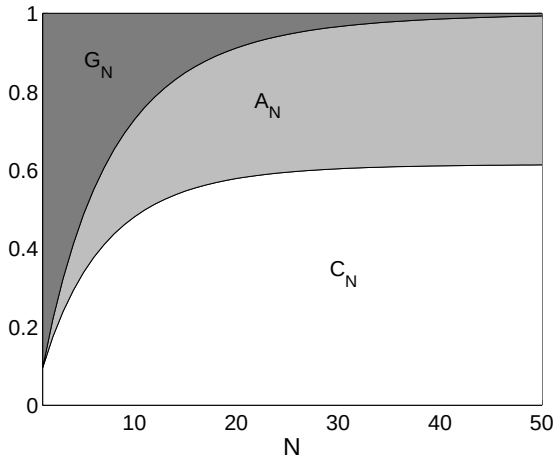

Fig. 16. Ideal surface-roughened LED: intensity channels C_N, A_N and G_N vs. number of bounces N.

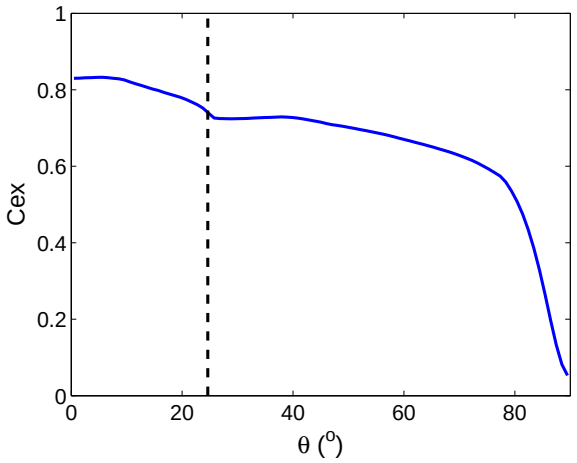

Fig. 17. $C_{ex}(\theta)$ for an ideal thin-film LED. The critical angle for a GaN/air interface is shown by the vertical line: $C_{ex}(\theta)$ decreases beyond this angle.

(round-trips) in the LED. After summing all light bounces in the LED, we obtain:

$$C_N = T \cdot \sum_{n=1..N} (R_p \cdot S)^{N-1} \cdot I \tag{6}$$

$$A_N = (1 - R_p) \cdot \sum_{n=2..N} (R_p \cdot S)^{N-2} \cdot S \cdot I \tag{7}$$

$$G_N = S \cdot (R_p \cdot S)^{N-1} \cdot I \tag{8}$$

Where C_N is the total intensity extracted after the N^{th} bounce, A_N is the total intensity absorbed in the $p-$ mirror after the N^{th} bounce, G_N is the intensity still guided in the structure after the N^{th} bounce (all these are column vectors indexed by θ) and $T = 1 - S$ is the transmission matrix of the rough surface. R_p is a diagonal matrix whose coefficients are the angle-resolved reflectivity (they are constant in our case since R_p is isotropic, but a more realistic Fresnel-type reflectivity can be used). In C_N and A_N, each term n in the sum corresponds to the contribution of the n^{th} bounce. Energy conservation after N bounces reads:

$$\int (C_N + A_N + G_N) d\Omega = \int I d\Omega = 1 \tag{9}$$

The final extraction C_{ex} and absorption A are the limits of C_N and A_N for $N \to \infty$ (obtained in practice for large N). Fig. 16 shows how C_N converges to C_{ex} after multiple bounces. For our example, we obtain $C_{ex} = 61.5\%$ and $A = 38.5\%$.

Following a photon gas approach, we can define an 'average number of bounces' N in the structure, so that $R_p^N = C_{ex}$. This yields $N \sim 9.5$. However, this number ignores the angular dependence of extraction.

Deeper insight in the behavior of light extraction can be gleaned by considering the angle-resolved extraction $C_{ex}(\theta)$. Here, θ designates the *initial angle of emission* of light. After it is emitted at a given angle θ, light is progressively scattered and extracted; $C_{ex}(\theta)$ indicates the final fraction of the emitted light which is extracted after all bounces and scatterings are taken into account. The total extraction efficiency C_{ex} is therefore related to $C_{ex}(\theta)$ by:

$$C_{ex} = \int C_{ex}(\theta) I(\theta) d\Omega \tag{10}$$

Fig. 17 shows $C_{ex}(\theta)$: as expected, extraction is strongly angle-dependent. It is maximal near normal incidence and decreases at larger θ. In this geometry with infinite lateral extension, sidewall extraction is not possible and C_{ex} vanishes at $\theta = 90^o$. Interestingly, the critical angle for extraction to air ($\theta_c \sim 26^o$) can still be observed in Fig. 17. As we saw in Sec. II, although the critical angle is no longer formally defined for a rough surface, there still exists a kink in the scattering profile around the critical angle; this kink produces a decrease in $C_{ex}(\theta)$ beyond θ_c.

We can also define an angle-dependent average number of bounces $N(\theta)$ before extraction, such that $R_p^{N(\theta)} = C_{ex}(\theta)$. The result is shown on Fig. 18. Near normal incidence, light escapes after ~ 4 bounces but this quantity diverges at large angle. Clearly, the concept of a constant number of bounces is not well suited to represent light extraction in this structure.

Finally, we conclude this discussion with a comment on the ergodicity of the system. Fig. 19 shows the relative intensity still guided in the structure, after N bounces. This quantity is defined as $G_N(\theta)/I(\theta)$, *i.e.* the ratio of light guided at bounce N to the initial emitted light. Overall, the intensity drops with N as light is extracted and absorbed. However, the intensity distribution is angle-dependent: intensity is concentrated at large angles, where light is not well scattered. Contrary to what one would expect in a photon gas model, [6] ergodicity *decreases* with successive bounces: starting from an isotropic distribution, we observe a pronounced intensity peak at large angle after only 3 bounces.[6]

[6]We even observe that the relative intensity goes slightly above unity at large angle for $N = 1$. This is because the large-angle light is mostly reflected, and some of the smaller-angle light is scattered to large angles.

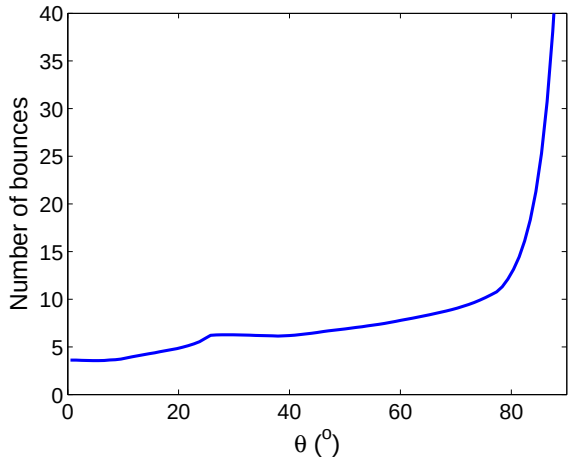

Fig. 18. Number of bounces before extraction, as a function of emission angle.

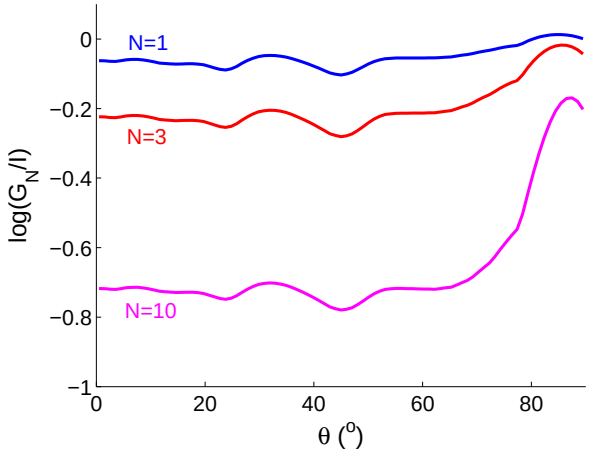

Fig. 19. Relative intensity in the LED as a function of θ after $N = 1, 3, 10$ bounces. Intensity decreases overall, but becomes concentrated at large angles.

C. Realistic light extraction model

After this study of an idealized structure, we turn our focus to realistic LEDs (i.e. taking into account the finite lateral extent of the LED and all its geometric features). In order to obtain extraction efficiency, we now need to integrate our results on scattering to a full LED model. We do so by coupling the scattering behavior of the rough surface to a raytracing model, as sketched in Fig. 20. In this approach, rays propagate according to geometric optics inside the chip until they impinge on the scattering surface. A set of scattered rays is then generated and injected back in the raytracing models. Because of the randomization by the rough surface, we work on field intensities rather than amplitudes ($i.e.$ as already mentioned, we make the reasonable hypothesis that phase is scrambled by the corrugation).

An important advantage of this approach is the reduced computation load, brought by decoupling the rough surface scattering problem from the LED extraction problem. The time-intensive solution of the scattering properties of the rough surface only has to be computed once (for a given type of roughness). The result can then be employed in a variety of LED simulations, where geometry and parameters are varied.

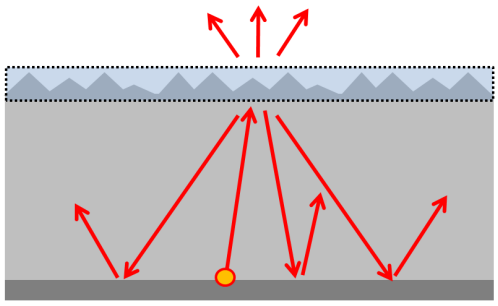

Fig. 20. Sketch of a raytracing model incorporating a rough surface. Rays propagate according to geometric optics inside the chip. When they meet the rough surface they are scattered according to our model, creating an additional set of rays in the raytracing engine.

Depending on the desired level of details, several approximations or refinements can be considered:

- Simple scalar reflectivities, or full (angle-dependent) Fresnel reflectivities and losses for the various interfaces
- Separate consideration of TE/TM polarizations or polarization averaging
- Inclusion of dipole source terms and cavity effects [24]–[28]
- Inclusion of the full angle-dependent diffuse scattering (e.g. diffuse intensity $R(\theta, \theta')$ as a full function of the incoming and outgoing angles), or simplification of the diffuse component to a Lambertian profile (e.g. $R(\theta) = R_s(\theta) + R_d$ where R_d is Lambertian).[7]
- Consideration of photon recycling of absorbed light

We have implemented this approach by coupling the surface scattering result to an in-house raytracing engine. By optimizing the coupled raytracing/scattering engine, we have obtained a fast code which is able to predict extraction efficiency in a realistic LED – we obtain a numerical accuracy better than 1% with a calculation time of one to a few minutes on a personal computer.

Our code can consider a detailed LED geometry, with smooth or rough interfaces. For smooth interfaces, each material's refractive index is specified and the angle-dependent Fresnel reflectivity is computed (this is of importance not only for dielectric interfaces but also for metallic mirrors, whose reflectivity can vary significantly with angle). Light emission is integrated over the source's position and over solid angles, and incorporates a realistic dipole emission diagram [24], [25], [28]. Various quantities (light extraction, loss in each material) are computed as a function of source position and solid angle, then integrated to yield net quantities. For most practical purposes, we have found that it is sufficient to average over polarizations and to simplify the diffuse scattering R_d to a Lambertian profile. On the other hand, it is of course crucial to distinguish the diffuse and specular components R_d and R_s.

[7]While the diffuse emission pattern of a rough surface integrated over all incoming angles θ is usually Lambertian, this is not necessarily the case for a specific angle of incidence. This approximation can be seen as a form of detailed sum.

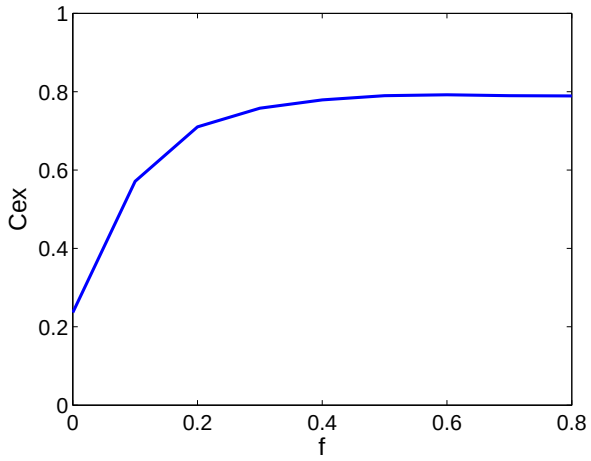

Fig. 21. C_{ex} as a function of the scattering strength f. The LED is a thin-film where the only source of loss is the $p-$mirror, for which we assume a reflectivity $R_p = 95\%$.

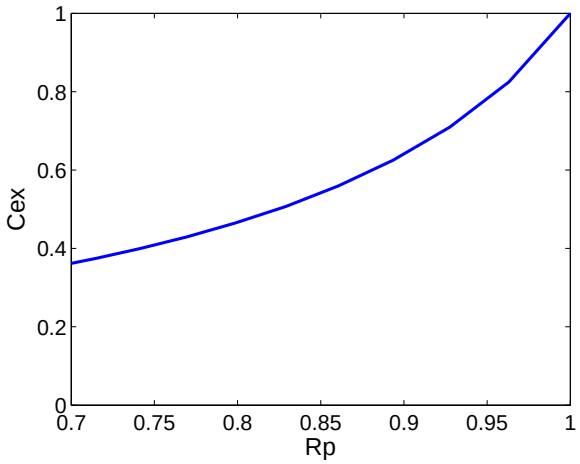

Fig. 22. C_{ex} as a function of $p-$metal reflectivity R_p.

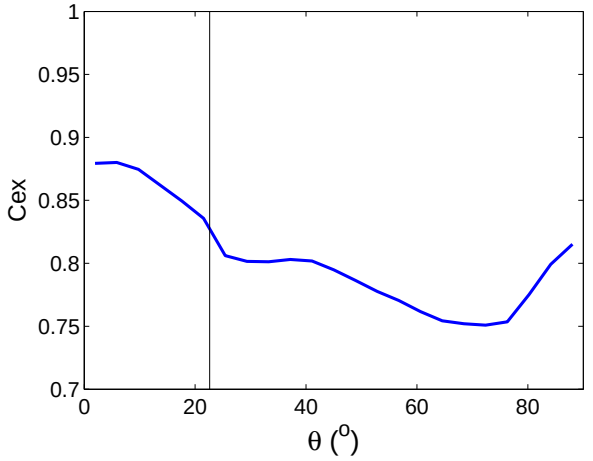

Fig. 23. $C_{ex}(\theta)$ for a simple thin-film LED. The critical angle for a GaN/air interface is shown by the vertical line.

D. Thin-film LEDs

In this section, we discuss light extraction in thin-film GaN LEDs where the GaN layer is about $5\mu m-$thick.

1) Simple geometry: We first consider a simplified thin-film LED made of GaN (thickness $5\mu m$, lateral extension $500\mu m$) whose only geometrical features are the $p-$mirror and surface roughness. The key parameters in this case are the scattering efficiency f of the surface and the reflectivity R_p of the $p-$mirror. Fig. 21 shows the extraction efficiency as a function of the scattering strength f of the rough surface. We assume a $p-$mirror reflectivity $R_p = 95\%$, which corresponds to a high-quality Ag reflector.[8] $f = 0$ corresponds to a smooth LED (in which microcavity effects [26], [27] are ignored for simplicity, although they could readily be incorporated in our approach) and increasing f corresponds to increasing roughness.

Increasing f at first significantly improves C_{ex}. Beyond $f = 0.4$ however, an asymptote is reached and further increase of f has no impact on C_{ex}. This is because, despite small changes in the backscattering profile for $f > 0.4$, the general trend of increased specular reflection at large angle always holds and dominates the limit value of extraction. This result suggests that the surface coverage of the corrugation is somewhat forgiving if roughness is sufficient. This prediction is different from what would be obtained if the rough surface was described in a geometric approach, where the existence of non-roughened areas impacts extraction; this is discussed in Appendix A.

We now choose an efficient scattering ($f = 0.4$) and study the impact of optical losses. Fig. 22 shows the extraction efficiency as a function of the $p-$mirror reflectivity R_p. The impact of R_p on C_{ex} is very strong – this is expected as several bounces are necessary before light gets extracted.

The angle-dependent extraction $C_{ex}(\theta)$ is shown on Fig. 23. In good agreement with our qualitative discussion in Sec. III-A, C_{ex} is maximal near normal incidence and decreases at larger angles, before partially recovering at very large angles thanks to partial sidewall extraction. Here again, we observe a kink in C_{ex} at $\theta = \theta_c$. We note that the sidewall contribution to extraction depends on the aspect ratio of the LED (a larger thin-film LED, such as a $1 \times 1mm^2$ chip, would benefit less from this effect). As already mentioned, the complex angle-dependent behavior of $C_{ex}(\theta)$ would be lost in a photon gas model. We note that the angular dependence is rather mild in this example: this is because the only source of loss is the high-reflectivity $p-$mirror, whose Fresnel reflectivity converges to unity for large angles – therefore partially compensating the reduced scattering efficiency of the rough surface at large angles.

2) Realistic geometry: In fact, thin-film LEDs incorporate multiple geometric features such as $n-$ and $p-$contacts, dielectric and metal streets near the edge of the device... We now consider a more realistic device: it also includes a grid $n-$electrode (located on the bottom side, in a flip-chip configuration). This grid has a reflectivity $R_n = 25\%$ and

[8]This is the normal-incidence reflectivity. Reflectivity varies with angle (with a Fresnel-coefficient behavior), and increases towards unity at large angle.

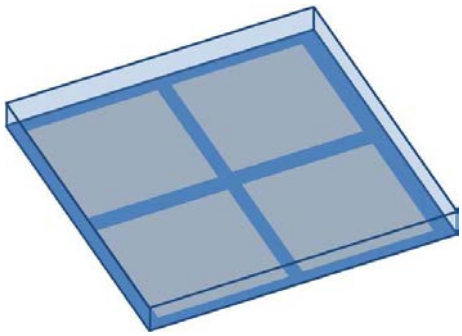

Fig. 24. Geometry of a realistic thin-film chip. The chip height is $5\mu m$, its lateral size $500\mu m$. The top of the chip is roughened. The bottom is covered by a $p-$mirror ($R_p = 95\%$) and an $n-$grid ($R_n = 25\%$) of width w.

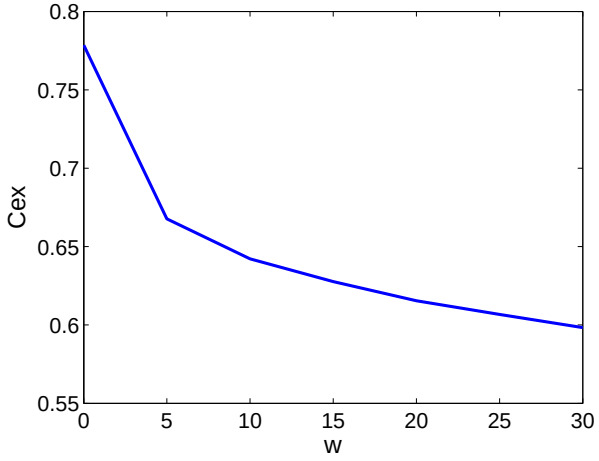

Fig. 25. C_{ex} as a function of w, for a realistic thin-film LED geometry.

a varying width w. Fig. 24 depicts the device. Of course, the actual dimensions of such lossy elements will vary in commercial devices. We merely intend here to illustrate how the addition of lossy features impacts C_{ex}. In the following calculations, light is only emitted above the $p-$contact (away from the $n-$grid).

Fig. 25 shows the resulting light extraction. Here we assume optimistic parameters $f = 0.4$ and $R_p = 95\%$, and compute C_{ex} as a function of w. The lossy $n-$grid has a significant impact on C_{ex}: even for $w = 5\mu m$ (an $n-$grid occupying less than 4% of the LED's total area), C_{ex} decreases by $\sim 10\%$.

To shed insight on these results, we represent on Fig. 26 the angle-dependent extraction $C_{ex}(\theta)$ for $w = 25\mu m$. As in Fig. 23 extraction generally decreases with large angles. However, the impact of the lossy features strongly enhances the effect. This is because large-angle light travels a long distance before it is extracted, and is therefore likely to impinge on lossy features.

Finally, Fig. 27 shows the local extraction efficiency (e.g. as a function of emission position). As expected, loss is highest for emission close to the n-grid.

From this discussion, we conclude that the presence of any lossy feature in a thin-film LED can have a significant impact on extraction $-$ often much more than what may be expected from the small surface coverage of such features.

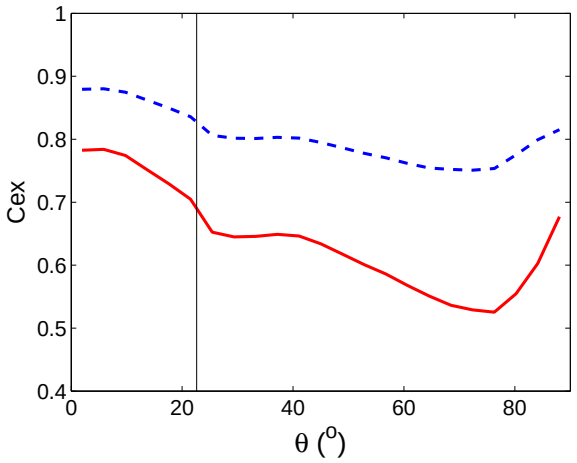

Fig. 26. $C_{ex}(\theta)$ for a simple thin-film LED (dashed line) and a realistic thin-film LED with $w = 25\mu m$ (full line). The critical angle for a GaN/air interface is shown by the vertical line.

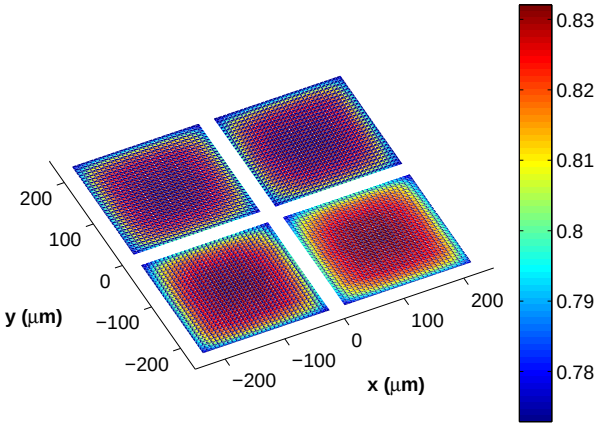

Fig. 27. C_{ex} vs. position for a realistic thin-film LED. Emission only occurs above the $p-$contact. Extraction is lowest close to the absorbing n-grid.

This is directly related to the scattering behavior of the rough surface: large-angle light is poorly scattered and has to travel a long distance in the LED before extraction, making it prone to interaction with lossy features. This provides incentive for reducing the presence of lossy elements to reach ultimate extraction efficiency. We also note that near $\theta \sim 90^o$, sidewall extraction slightly helps C_{ex}.

3) Effect of encapsulation: In Section II-G, we showed how the scattering properties of a rough surface depended on the index of the output medium (air or encapsulant). We now study how this affects C_{ex}.

We consider a realistic thin-film die as above, with $w = 10\mu m$. C_{ex} is shown on Fig. 28 as a function of R_p, both for extraction to air and to an encapsulant ($n = 1.4$). As expected, C_{ex} increases with encapsulation. We note that for $R_p = 95\%$, we obtain $C_{ex} \sim 65\%$ in air and $\sim 80\%$ encapsulated. These values are close to those reported in Ref. [1], which is one of the few published experimental results on extraction efficiency

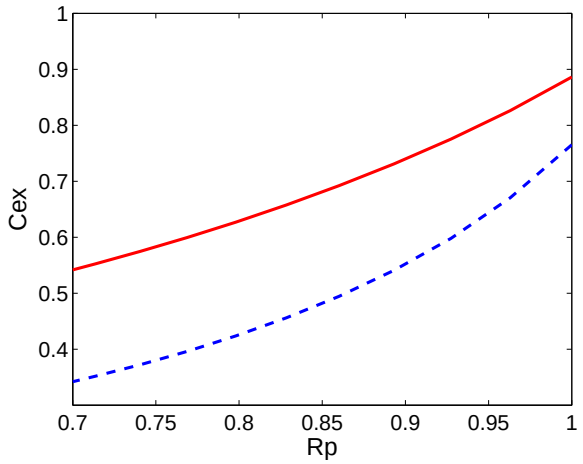

Fig. 28. C_{ex} as a function of R_p: impact of encapsulation. Dashed line: LED in air; full line: encapsulated LED ($n = 1.4$).

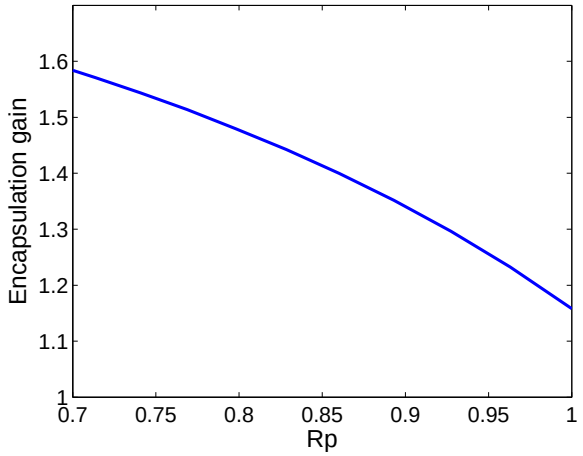

Fig. 29. Encapsulation gain as a function of R_p.

in a thin-film die.[9]

The ratio of the two extractions, called encapsulation gain, is plotted on Fig. 29. We see that the encapsulation gain decreases when R_p increases. This illustrate a well-known trend: a large encapsulation gain is indicative of a lossy die. This is because extraction to air requires more bounces than extraction to an encapsulant, making the impact of any additional loss more pronounced. For a good reflector $R_p = 0.9$, we obtain an encapsulation gain of ~ 1.3 which is in the range of typical values reported by LED manufacturers [1].

E. Volumetric chips

So far we have considered thin-film chips, whose vertical dimensions are on the order of a few μm. We now discuss light extraction in volumetric chips, whose height is in the range of a few tens to a few hundreds of μm. As we will see, the main difference between thin-film and volumetric chips

[9]The geometry of the die we considered is not specifically designed to mimic that of Ref. [1]; however the similar C_{ex} values suggest that the overall balance of scattering and optical loss is of a similar order.

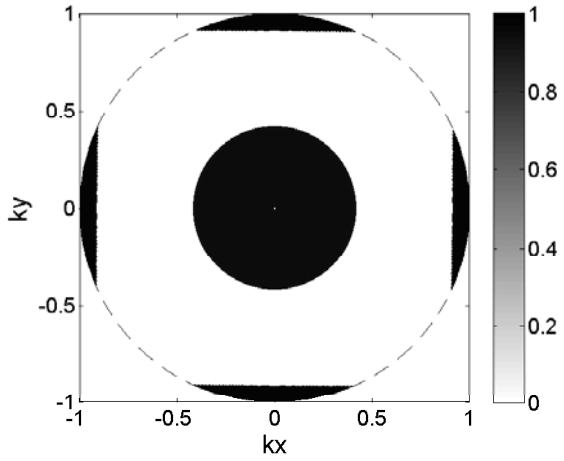

Fig. 30. Angle-resolved extraction diagram $C_{ex}(\theta, \varphi)$ for a square volumetric chip. Extraction is only possible in the top extraction cone and the four side extraction cones; in these cones, extraction is near unity. The dashed line corresponds to $\theta = \pi/2$, $i.e.$ to the boundary of the polar plot.

is that the latter enable extraction through their sidewalls. By coupling this geometric contribution to surface roughness, higher extraction values can be obtained.

1) Non-roughened volumetric chip: We start our discussion by considering non-roughened volumetric dies, where the geometry of the die alone is used to increase light extraction.

The simplest form of volumetric die is the cubic die. For light emitted anywhere at the base of the LED, a cubic die provides six extraction cones (one for each sidewall, and two for the top surface due to reflection by the $p-$mirror). If the solid angle subtended by one extraction cone is Ω_c, the expected extraction is therefore roughly $C_{ex} \sim 6\Omega_c/4\pi$. In the case of a cubic GaN LED, we obtain $C_{ex} \sim 25\%$. The actual value is slightly different because of partial Fresnel reflections at the interfaces, finite reflectivity of the $p-$mirror, absorption in the substrate and of the radiation diagram of the LED's active region. For instance, if we consider a cubic GaN LED of size $250\mu m$ with a bulk absorption $\alpha = 1cm^{-1}$ and a $p-$mirror with $R_p = 95\%$, a raytracing calculation yields $C_{ex} = 23.8\%$.[10]

We now consider the angle-resolved extraction diagram of the structure $C_{ex}(\theta, \varphi)$ (e.g. the final extraction for light initially emitted at angle (θ, φ), integrated over all source positions). This quantity is similar to $C_{ex}(\theta)$ defined earlier, but due to the sidewall contribution extraction now depends on φ as well as θ. We represent $C_{ex}(\theta, \varphi)$ as a polar plot on Fig. 30 (where $k_x = \sin\theta\cos\varphi$ and $k_y = \sin\theta\sin\varphi$ are the polar coordinates of light emission).

The extraction cones corresponding to the five facets of the LED are seen as dark spots (with $C_{ex} \sim 1$) on Fig. 30. The central spot is a circle, and corresponds to the top facet's extraction cone. The four side facets appear as narrow bands of extraction in the corresponding in-plane directions. We note that, although the area of these bands looks small they subtend the same solid angle as the top extraction cone (their projected

[10]This value is close to the simpler estimate because the use of a realistic radtiation diagram partially cancels out the effect of losses.

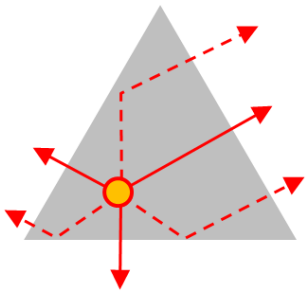

Fig. 31. Top-view sketch of a triangular LED showing two sets of ray trajectories. Light is extracted directly when it is directed towards a facet (full line), or after one bounce when it is directed to the opposite direction (dashed line). Therefore, the three sidewalls provide six cones for extraction.

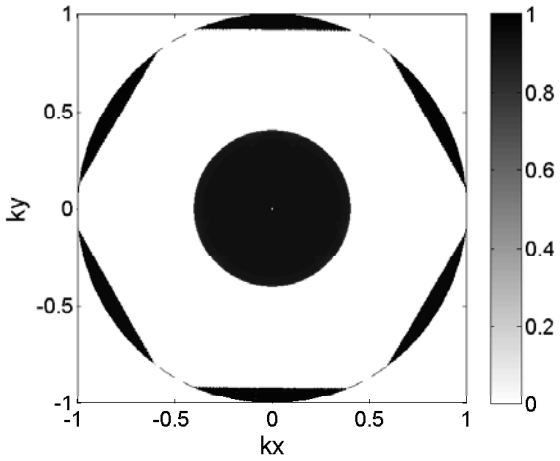

Fig. 32. $C_{ex}(\theta,\varphi)$ for a triangular volumetric chip. Here each sidewall provides two extraction cones (for light impinging on the sidewall immediately, or after one bounce) yielding six lateral extraction cones.

area merely appears smaller in this polar representation). Light outside these extraction cones is never extracted whereas extraction in the cones is near unity (due to the low optical loss for such light) – hence the 'digital' appearance of Fig. 30.

To improve on the performance of a cubic LED, one can shape the chip as an equilateral triangle. In this case, each of the triangle's sidewalls contributes two extraction cones, as explained on Fig. 31. Therefore, a rough estimate of extraction is $C_{ex} \sim 8\Omega_c/4\pi \sim 33.4\%$ for a GaN LED. In fact we obtain $C_{ex} = 29.8\%$ with a raytracing calculation and the same parameters as above.The corresponding angle-resolved extraction diagram $C_{ex}(\theta,\varphi)$ is shown on Fig. 32. As expected, six ectraction cones now appear in the six in-plane directions corresponding to sidewall extraction.

Obviously, many more geometrical shapes can be considered – some of which are very efficient, leading to extraction efficiencies on par with thin-film surface-roughened LEDs. Important references in this field are Refs. [29], [30]; further investigation of chip-shaping in GaN LEDs was carried out in Ref. [31]. While efficient, such shapes are more complex to manufacture (they require processing steps such as slanted sawing, which can be costly and time-consuming). We do not discuss this approach further here as it is not the object of this work.

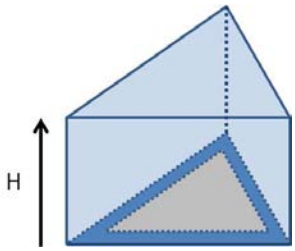

Fig. 33. Sketch of a flip-chip volumetric die incorporating a $p-$mirror and an $n-$grid.

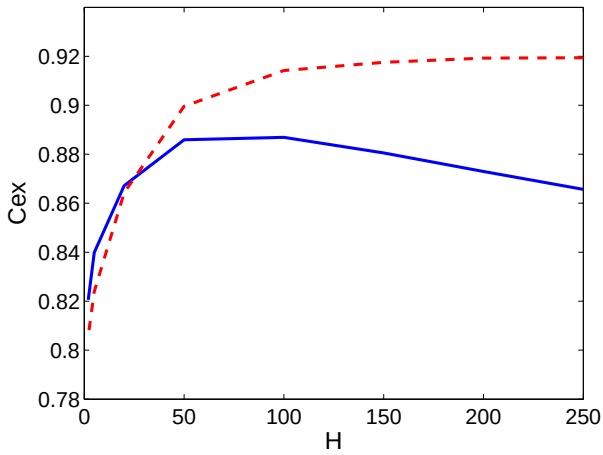

Fig. 34. C_{ex} vs. chip thickness H, for an encapsulated triangular chip with a roughened top surface. Full: no sidewall roughness. Dashed: sidewall roughness.

2) Surface-roughened volumetric chip: We now consider chips which combine a volumetric/geometrical approach and surface roughness, and study how the two light-extraction strategies can be combined. Our starting point is the triangular chip described above, encapsulated in a medium of index $n = 1.4$. We assume a $p-$mirror reflectivity $R_p = 95\%$, as well as an absorbing $n-$ electrode belt around the $p-contact$, of thickness $5\mu m$ and reflectivity $R_n = 25\%$. We allow the chip height to vary from $2\mu m$ (corresponding to a thin-film regime) to $250\mu m$. The chip geometry is sketched on Fig. 33.

Fig. 34 displays the corresponding extraction: C_{ex} increases with H thanks to the additional extraction provided by the sidewalls. While sidewall extraction is not totally absent from thin-film chips, it is limited because large-angle light has to bounce many times before reaching the chip's extremities. In the volumetric case, light reaches the edges of the chip after one or two bounces only. In our example, the volumetric case improves on the thin-film by $\sim 6-7\%$, a significant increase in this regime where extraction is already high. An experimental demonstratrion of high-efficiency LEDs using this architecture was recently reported in Ref. [32].

We also observe that C_{ex} is maximal around $H \sim 100\mu m$ and slightly decreases beyond this point: this is due to the substrate absorption loss α, which has more influence for tall chips. To clarify this, the balance of optical losses is illustrated on Fig. 35. With increasing thickness, loss in the $p-$mirror

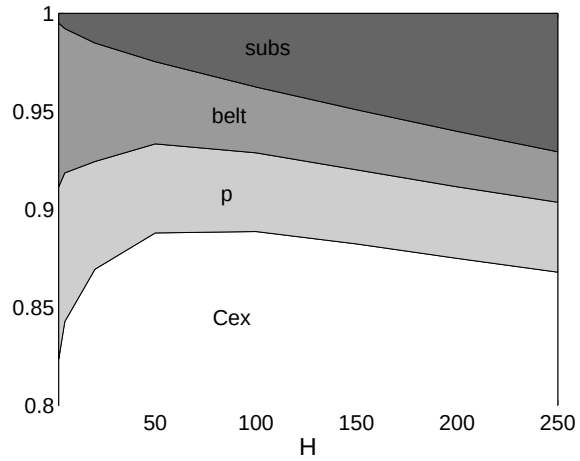

Fig. 35. Cumulative plot of extraction and losses in a roughened triangular chip, vs. chip height H. The loss channels are the $p-$mirror, the lossy $n-$grid and the substrate absorption.

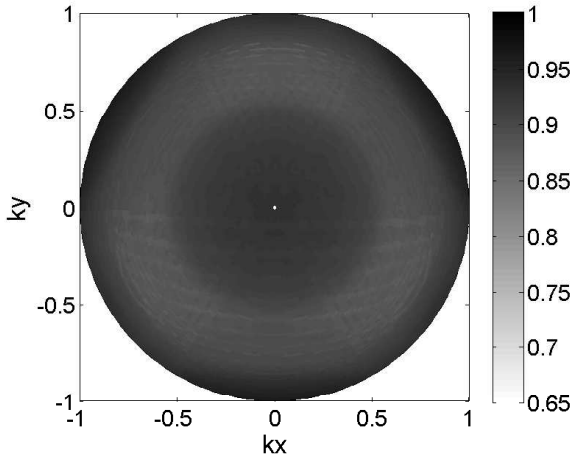

Fig. 37. $C_{ex}(\theta,\varphi)$ for a triangular volumetric chip with top and sidewall surface roughness. Light is extracted at all angles with an efficiency above 88%.

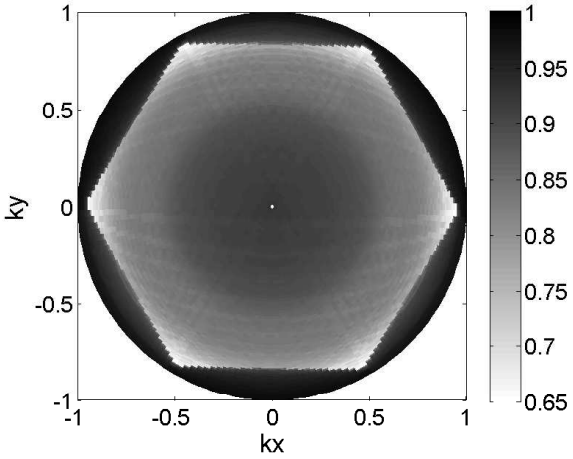

Fig. 36. $C_{ex}(\theta,\varphi)$ for a triangular volumetric chip with top surface roughness. Light outside the extraction cone of the facets is now extracted, although some directions are still not perfectly extracted.

and the absorbing $n-$contact decrease. This is because light is extracted by the sidewalls with fewer bounces on these elements. At the same time, substrate absorption increases because light travels a longer distance in the lossy substrate. The optimal value of H generally depends on α and the chip's other dimensions.

Finally, Fig. 36 shows the angle-resolved extraction diagram $C_{ex}(\theta,\varphi)$ for a surface-roughened triangular chip with $H = 100\mu m$. As in Fig. 32, the six extraction cones corresponding to the sidewalls are still clearly observed. The extraction cone corresponding to the top facet is now smeared out, because roughness slightly decreases extraction at normal incidence and allows extraction beyond the critical angle.

3) Sidewall-roughened volumetric chip: As seen in Fig 36, light extraction is nearly ideal in a wide range of angles but still imperfect at intermediate angles (especially at large θ angles, in-between the facets' extraction cones). Further improvement in light extraction can be obtained by adding sidewall roughness to this chip. Fig. 34 shows how C_{ex} varies with chip height in this case. In the thin-film limit, sidewall roughness brings no benefit since light hardly reaches the sidewalls. In the volumetric regime on the other hand, extraction can be further enhanced by 4%. Interestingly, C_{ex} keeps increasing for $H > 100\mu m$ in this case, because light escapes after fewer bounces (hence mitigating the effect of substrate absorption).

Fig. 37 displays $C_{ex}(\theta,\varphi)$ in such a structure for $H = 100\mu m$. We use the same color scale as in Fig. 36 for comparison. Here all angles are extracted with an efficiency higher than 88%, yelding an extremely high extraction efficiency for this level of optical loss – most notably, the few angular sectors of low extraction seen in Fig. 36 are now efficiently extracted.

IV. Conclusion

We have presented a light scattering model which yields representative scattering profiles for micron-sized textured interfaces. The model is based on solving Maxwell's equations for sets of periodic corrugated structures and averaging these to obtain the emergent properties of the rough interface. The results were shown to be robust against the details of surface roughness. The key conclusion of this study is the strong dependence of scattering on the polar angle of light: light impinging on the rough surface at glancing angles undergoes strong specular reflection and little outcoupling. This behavior has important effects on light extraction. These results are general and independent of the details of the textured geometry, and as such apply to a variety of textured interfaces (including photonic-crystal LEDs, as argued in Ref. [21]).

By coupling this scattering model with a raytracing model, we predicted realistic trends of extraction efficiency in surface-roughened LEDs. In thin-film LEDs, optical losses dictate extraction efficiency; due to the long travel distance of large-angle light, the impact of lossy elements is higher than would be expected from their surface coverage. Finally, we showed

how combining surface roughening with a volumetric architecture enables light extraction to be significantly improved beyond the thin-film case, by ensuring efficient extraction of large-angle light.

From a more general standpoint, we conclude that optical devices integrating rough interfaces can not always be assumed to fulfill the condition of ergodicity which warrants the use of the common photon gas model. The breakdown of ergodicity can be traced down to two effects: 1) an efficient extraction scheme ensures that at least some angles will escape very quickly (sometimes after 1-2 bounces), thus violating the assumption that all light bounces many times inside the structure and 2) some angles, on the other hand, are poorly outcoupled and see an accumulation of light. These effects yield an imbalance in the angular distribution of light inside the structure. In situations where ergodicity is not met, optical properties can become non-trivial and care should be taken to optimize the device in accordance with the scattering properties. This may be of importance in a variety of optical systems such as LEDs, organic LEDs and photovoltaic cells.

APPENDIX A
COMPARISON TO GEOMETRIC OPTICS

Here we compare two approaches to compute scattering by a rough surface: wave optics and geometric optics. Indeed, geometric optics have sometimes been used to predict light extraction from surface-roughened GaN LEDs and one may wonder whether this is warranted given the micron-scale feature size of such surfaces. The wave-optics approach, on the other hand, is expected to be safely applicable in the considered regime (it only assumes the lateral coherence of the incoming plane wave over distances larger than the typical scale of the corrugation, which is clearly the case).

We consider a roughened GaN surface of infinite lateral extent, encapsulated in a high-index material ($n = 1.4$) with a corrugation of conical pyramids as in Fig. 8. The pyramids have a top angle of 60^o, and sit on a triangular lattice with a large filling fraction $f = 0.9$. In the raytracing calculation, the top angle of the pyramids fully specifies the geometry; rays are generated at all angles and single-bounce extraction is computed. For the wave approach, we use the scattering matrix algorithm as in the rest of this article. Unlike the geometric case, the relative frequency $u = a/\lambda$ has to be specified (with larger u corresponding to larger pyramids). The pyramids are approximated by 20 cylindrical slices, as sketched in Fig. 7. We take care to use proper Fourier factorization rules to ensure numerical convergence [33]. We retain 367 harmonics waves in the Fourier decompositions, which ensures numerical convergence up to $u = 4.5$.

Fig. 38 shows the total backscattering $R(\theta)$ (integrated over the azimuthal angle φ) for both approaches. As u increases, the wave-optics calculations describes larger feature sizes and its result slowly converges towards the geometric result. For $u = 1.5$ the wave-optics result and the geometric result are quite different, while they are in better agreement for $u = 4.5$. However convergence is not complete even for this high frequency – corresponding to a lateral pitch $a \sim 2\mu m$,

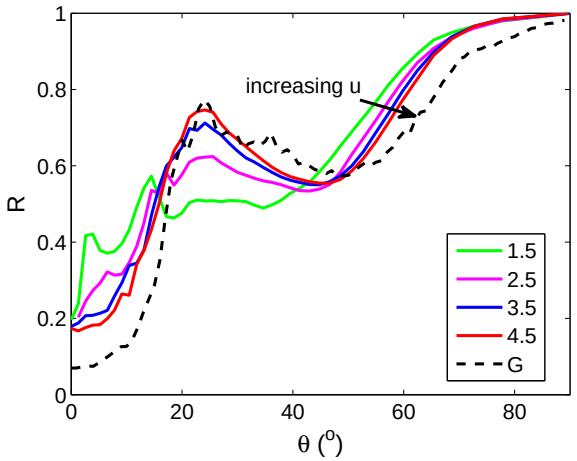

Fig. 38. Convergence of wave optics calculations towards the geometric limit with feature size. The full curves are S-matrix calculations with increasing values of $u = 1.5 - 4.5$. They slowly converge towards the geometric limit (dashed line).

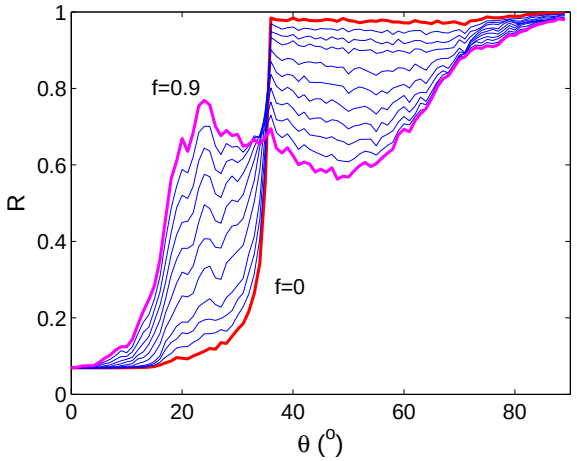

Fig. 39. Effect of filling fraction f in a geometric calculation. The thick lines highlight the cases $f = 0$ (smooth interface, where the Fresnel reflectivity is recovered modulo numerical inaccuracies) and $f = 0.9$ (nearly-maximal value). For intermediate values of f, R can be obtained as a weighed average of these two results. All intermediate curves present a kink at the critical angle, inherited from the $f = 0$ curve.

on the higher end of what is usually observed in surface-roughened GaN. This is in line with known results for the convergence of wave optics: in the case of Mie scattering by spheres, the geometric limit is only attained for very large radii (several tens of optical wavelengths) [34]. We did not push our calculations to higher values of u, as this would require more harmonics and make the calculation time prohibitive.

Geometric optics also fail at fully describing some scattering trends such as the dependence on the filling fraction of the roughness. In the geometric approach, scattering for intermediate f values is trivially obtained by a weighed averaged of the scattering with high f, and the Fresnel reflectivity of a smooth surface (because light beams either impinge on the pyramids or on the flat surface). Fig. 39 illustrates this result. Some features of the resulting R are a kink at the critical angle and a slow

convergence towards a smooth profile with increasing f. These results should be contrasted with what is obtained in a wave-optics calculation (Fig. 6), where R is smooth for all values of f (except $f = 0$) and where all values of $f > 0.4$ yield similar R and similar extraction efficiency (Fig. 21). This suggests that the geometric approach overestimates the detrimental impact of an imperfectly roughened surface.

We conclude that the geometric approach yields scattering results which are to some extent similar to a full wave-optics treatment, but also presents differences. The validity of the geometric limit is therefore not fully clear: it may be expected to yield qualitatively correct extraction predictions, but quantitative agreement is less certain.

REFERENCES

[1] M. R. Krames, O. B. Shchekin, R. Mueller-Mach, G. O. Mueller, L. Zhou, G. Harbers, and M. G. Craford, "Status and future of high-power light-emitting diodes for solid-state lighting," *Journal of Display Technology*, vol. 3, no. 2, pp. 160–175, 2007.

[2] I. Schnitzer, E. Yablonovitch, C. Caneau, T. J. Gmitter, and A. Scherer, "30% external quantum efficiency from surface textured, thin-film light-emitting diodes," *Applied Physics Letters*, vol. 63, no. 16, pp. 2174–2176, 1993.

[3] T. Fujii, Y. Gao, R. Sharma, E. L. Hu, S. P. DenBaars, and S. Nakamura, "Increase in the extraction efficiency of GaN-based light-emitting diodes via surface roughening," *Applied Physics Letters*, vol. 84, no. 6, pp. 855–857, 2004.

[4] O. B. Shchekin, J. E. Epler, T. A. Trottier, T. Margalith, D. A. Steigerwald, M. O. Holcomb, P. S. Martin, and M. R. Krames, "High performance thin-film flip-chip InGaN-GaN light-emitting diodes," *Applied Physics Letters*, vol. 89, no. 7, p. 071109, 2006.

[5] S. J. Lee, "Analysis of light-emitting diodes by Monte Carlo photon simulation," *Appl. Opt.*, vol. 40, no. 9, pp. 1427–1437, 2001.

[6] E. Yablonovitch, "Statistical ray optics," *J. Opt. Soc. Am.*, vol. 72, no. 7, pp. 899–907, 1982.

[7] H. W. Deckman, C. B. Roxlo, and E. Yablonovitch, "Maximum statistical increase of optical absorption in textured semiconductor films," *Opt. Lett.*, vol. 8, no. 9, pp. 491–493, 1983.

[8] M. Boroditsky, R. Ragan, and E. Yablonovitch, "Absorption enhancement in ultra-thin textured AlGaAs films," *Solar Energy Materials and Solar Cells*, vol. 57, no. 1, pp. 1–7, 1999.

[9] M. Boroditsky and E. Yablonovitch, "Light-emitting-diode extraction efficiency," in *Proc. Spie*, vol. 3002, 1997, pp. 119–122.

[10] R. Windisch, S. Schoberth, S. Meinlschmidt, P. Kiesel, A. Knobloch, P. Heremans, B. Dutta, G. Borghs, and G. H. Dohler, "Light propagation through textured surfaces," *Journal of Optics A: Pure and Applied Optics*, vol. 1, no. 4, p. 512, 1999.

[11] R. Windisch, M. Kuijk, B. Dutta, A. Knobloch, P. Kiesel, G. H. Doehler, G. Borghs, and P. L. Heremans, "Nonresonant-cavity light-emitting diodes," *Proc. SPIE*, vol. 3938, pp. 70–76, 2000.

[12] R. Windisch, C. Rooman, B. Dutta, A. Knobloch, G. Borghs, G. H. Dohler, and P. Heremans, "Light-extraction mechanisms in high-efficiency surface-textured light-emitting diodes," *Selected Topics in Quantum Electronics, IEEE Journal of*, vol. 8, no. 2, pp. 248–255, 2002.

[13] F. E. Nicodemus, J. C. Richmond, J. J. Hsia, I. W. Ginsberg, and T. Limperis, "Geometric considerations and nomenclature for reflectance," 1977.

[14] D. M. Whittaker and I. S. Culshaw, "Scattering-matrix treatment of patterned multilayer photonic structures," *Physical Review B*, vol. 60, no. 4, pp. 2610–2618, 1999.

[15] S. G. Tikhodeev, A. L. Yablonskii, E. A. Muljarov, N. A. Gippius, and T. Ishihara, "Quasiguided modes and optical properties of photonic crystal slabs," *Physical Review B*, vol. 66, no. 4, p. 045102, 2002.

[16] K. E. Torrance and E. M. Sparrow, "Theory for off-specular reflection from roughened surfaces," *Journal of the Optical Society of America*, vol. 57, no. 9, p. 1105, 1967.

[17] X. D. He, K. E. Torrance, F. X. Sillion, and D. P. Greenberg, "A comprehensive physical model for light reflection," *Computer Graphics*, vol. 25, no. 4, 1991.

[18] S. K. Nayar, K. Ikeuchi, and T. Kanade, "Surface reflection - physical and geometrical perspectives," *IEEE Transactions on Pattern Analysis and Machine Intelligence*, vol. 13, no. 7, pp. 611–634, 1991.

[19] A. David, H. Benisty, and C. Weisbuch, "Optimization of light-diffracting photonic-crystals for high extraction efficiency LEDs," *Journal of Display Technology*, vol. 3, no. 2, p. 133, 2007.

[20] H. Benisty, P. Lalanne, S. Olivier, M. Rattier, C. Weisbuch, C. J. M. Smith, T. F. Krauss, C. Jouanin, and D. Cassagne, "Finite-depth and intrinsic losses in vertically etched two-dimensional photonic crystals," *Optical and Quantum Electronics*, vol. 34, no. 1-3, pp. 205–215, 2002.

[21] A. David, H. Benisty, and C. Weisbuch, "Photonic crystal light-emitting sources," *Reports on Progress in Physics*, vol. 75, no. 12, p. 126501, 2012.

[22] A. David, C. Meier, R. Sharma, F. S. Diana, S. P. DenBaars, E. Hu, S. Nakamura, C. Weisbuch, and H. Benisty, "Photonic bands in two-dimensionally patterned multimode GaN waveguides for light extraction," *Applied Physics Letters*, vol. 87, no. 10, p. 101107, 2005.

[23] A. David, T. Fujii, R. Sharma, K. McGroddy, S. Nakamura, S. P. DenBaars, E. L. Hu, C. Weisbuch, and H. Benisty, "Photonic-crystal GaN light-emitting diodes with tailored guided modes distribution," *Applied Physics Letters*, vol. 88, no. 6, p. 061124, 2006.

[24] H. Benisty, H. De Neve, and C. Weisbuch, "Impact of planar microcavity effects on light extraction - part I: Basic concepts and analytical trends," *IEEE Journal of Quantum Electronics*, vol. 34, no. 9, pp. 1612–1631, 1998.

[25] ——, "Impact of planar microcavity effects on light extraction - part II: Selected exact simulations and role of photon recycling," *IEEE Journal of Quantum Electronics*, vol. 34, no. 9, pp. 1632–1643, 1998.

[26] Y. C. Shen, J. J. Wierer, M. R. Krames, M. J. Ludowise, M. S. Misra, F. Ahmed, A. Y. Kim, G. O. Mueller, J. C. Bhat, S. A. Stockman, and P. S. Martin, "Optical cavity effects in InGaN/GaN quantum-well-heterostructure flip-chip light-emitting diodes," *Applied Physics Letters*, vol. 82, no. 14, pp. 2221–2223, 2003.

[27] C. Weisbuch, A. David, T. Fujii, C. Schwach, S. P. DenBaars, S. Nakamura, M. Rattier, H. Benisty, R. Houdr, R. Stanley, J. F. Carlin, T. F. Krauss, and C. J. M. Smith, "Recent results and latest views on microcavity LEDs," *Proceedings of the SPIE - The International Society for Optical Engineering*, vol. 5366, no. 1, 2004.

[28] A. David, "High efficiency GaN-based LEDs: light extraction by photonic crystals," *Annales de Physique*, vol. 31, no. 6, 2006.

[29] M. R. Krames, M. Ochiai-Holcomb, G. E. Hofler, C. Carter-Coman, E. I. Chen, I. H. Tan, P. Grillot, N. F. Gardner, H. C. Chui, J. W. Huang, S. A. Stockman, F. A. Kish, M. G. Craford, T. S. Tan, C. P. Kocot, M. Hueschen, J. Posselt, B. Loh, G. Sasser, and D. Collins, "High-power truncated-inverted-pyramid (AlxGa1-x)(0.5)In0.5P/GaP light-emitting diodes exhibiting $>$ 50 percent external quantum efficiency," *Applied Physics Letters*, vol. 75, no. 16, pp. 2365–2367, 1999.

[30] D. Ochoa, "Diodes electroluminescentes planaires a haut rendement d'extraction lumineuse," Ph.D. dissertation, EPFL, 2001.

[31] X. H. Wang, P. T. Lai, and H. W. Choi, "The contribution of sidewall light extraction to efficiencies of polygonal light-emitting diodes shaped with laser micromachining," *Journal of Applied Physics*, vol. 108, no. 2, p. 023110, 2010.

[32] M. J. Cich, R. I. Aldaz, A. Chakraborty, A. David, M. J. Grundmann, A. Tyagi, M. Zhang, F. M. Steranka, and M. R. Krames, "Bulk GaN based violet light-emitting diodes with high efficiency at very high current density," *Applied Physics Letters*, vol. 101, no. 22, p. 223509, 2012.

[33] A. David, H. Benisty, and C. Weisbuch, "Fast factorization rule and plane-wave expansion method for two-dimensional photonic crystals with arbitrary hole-shape," *Physical Review B*, vol. 73, no. 7, 2006.

[34] M. I. Mishchenko, L. D. Travis, and A. A. Lacis, *Scattering, Absorption and Emission of Light by Small Particles*. Cambridge University Press, 2002.

Aurelien David Aurelien graduated with a Masters in Quantum Physics from Ecole Polytechnique in 2003, and with a PhD in Applied Physics from Ecole Polytechnique in collaboration with the University of California, Santa Barbara in 2006. From 2006 to 2010 he worked in the Advanced Laboratories at Philips Lumileds. He joined Soraa, Inc. in 2010. His work is both theoretical and experimental; it focuses on semiconductor optics and physics, and aspects of III-Nitride LEDs efficiency.